IEEE Access
Multidisciplinary | Rapid Review | Open Access Journal

Received August 6, 2020, accepted September 30, 2020, date of publication October 6, 2020, date of current version October 15, 2020.

Digital Object Identifier 10.1109/ACCESS.2020.3028866

A Study of Wave Refraction in a Marginal Ice Zone: Frazil-Pancake Ice

HAIJIN DAI[1,2], JUN ZHAO[2], AND XUEYAN ZHANG[2]
[1]College of Oceanic and Atmospheric Sciences, Ocean University of China, Qingdao 266100, China
[2]College of Meteorology and Oceanography, National University of Defense Technology, Changsha 410073, China

Corresponding authors: Haijin Dai (hj_dai@nudt.edu.cn) and Jun Zhao (zhaojun@nudt.edu.cn)

This work was supported by the National University of Defense Technology under Grant ZK18-03-29.

ABSTRACT Theoretical estimates based on both offline calculation and an online model are made to study the wavenumber variations during wave refraction in a marginal ice zone (MIZ). Analysis of in situ observations from the MIZ of the Arctic Ocean confirms the conclusion drawn based on theoretical estimates as well as the simulation ability of our new model to describe wave evolution in the MIZ. In wave refraction, variation of wavenumber in magnitude is determined by the incident wavenumber and the ice mass. A larger incident wavenumber or a larger ice mass leads to a larger variation of wavenumber in magnitude, though during refraction, the variation of wavenumber in magnitude is more sensitive to the incident wavenumber because it is proportional to the cube of the incident wavenumber, while it is linearly proportional to the ice mass. On the other hand, both the angle of refraction and the deflection are determined by the angle of incidence, the incident wavenumber and the ice mass. A larger angle of incidence, a shorter wave or larger ice mass results in a larger angle of refraction and a larger deflection. All these conclusions are supported by offline calculations, an online model and in situ observations. The online model also suggests that the instrument should be kept at a distance from the ice edge to obtain more general information of the open ocean.

INDEX TERMS Wave refraction, marginal ice zone, frazil-pancake ice, wavenumber variation.

I. INTRODUCTION

An MIZ, which is defined as the transitional zone between packed ice and the open ocean [1], is an important zone for atmosphere-ocean-ice-wave interactions. Usually, an MIZ covers a vast distance of approximately 10-100 *km* from the edge of the frozen ocean to the open ocean, and it can even reach as far as 200 *km* into circumpolar Antarctica during the winter [2]. Two types of young ice (frazil ice and pancake ice) form in turbulent environments in the MIZ. When the water temperature is below the freezing point, new ice that appears as a slurry of sea spicules with no floe is called frazil ice. As frazil ice gradually thickens and consolidates, pancake ice forms with a diameter of 1-2 *m*. Because the thickness of frazil-pancake ice varies from several centimeters to over 1 *m*, its behavior can be accurately described by a mass-loading model [3].

Directly exposed to the open ocean, the MIZ is important for wave-ice interactions. When surface gravity waves reach the ice zone, some penetrate deeply, whereas others are reflected back into the open ocean. Both the transmission rate and the reflection rate are determined by the ice thickness, the angle of incidence, the incident wavenumber and the refracted wavenumber [4], [5]. Wadhams [2] suggested that the reflection rate rapidly decreases with increasing wavenumber. It was also suggested that when the ice is less than 1 *m* thick, the reflection rate is usually too small to consider. In this study, reflection is always neglected based on the features of the ice and the waves. As the surface gravity waves reach the ice zone, the magnitude of the wavenumber and the propagation direction of the refracted waves change due to refraction. As the refracted waves propagate in the ice zone, the wave energy is dissipated not only by breaking and bottom drags [6] but also by sea ice, which is even more influential [7], [8]. A typical e-folding distance is 1-20 *km* according to the ice properties and the wavenumber [9]. However, with a low ice fraction and a strong amplitude in the Southern Ocean, a wave can propagate over several hundred kilometers in the MIZ before its energy dissipates completely [10]. As the energy dissipates, momentum is transferred to the

The associate editor coordinating the review of this manuscript and approving it for publication was Jenny Mahoney.

sea ice through radiation stress, which accelerates the sea ice, and eventually, the momentum is transferred into the current beneath the ice through interfacial stress [11], [12]. Eventually, ice-edge jets appear both in the sea ice and the current [3], [13].

Similar to previous studies, Dai [3] focused primarily on wave energy evolution and formulation of the ice-edge jet. Consistent with in situ observations, wave energy dissipation [13] and mesoscale eddy genesis [14] can be well demonstrated with our coupled ocean-ice-wave system. However, wave refraction always occurs due to the ice mass variation in space. Variation of wavenumber in magnitude and propagating direction during wave refraction were not discussed sufficiently in [3] (i.e., features of wavenumber increase and deflection), due to the topic preference in that paper. Furthermore, the coding for wavenumber evolution (wave refraction in the ice zone) in our model still needs to be verified with in situ observations, which were inadequate in the past. As increasing attention is paid to the physical processes in MIZs, a project was conducted with the aim of studying the boundary layer physics in the Arctic Ocean with many advanced instruments (moorings, wave buoys, satellites, etc.) [15], [16]. Recently, high-quality and continuous observations that describe the distribution of wave features were made available. Although their following analysis still focused on wave energy dissipation [17], they offered an opportunity for us to find out real physical process of wave refraction and verify the coding of wavenumber evolution in our coupled model.

Two questions are considered in this study. The first question is whether the wavenumber evolution is well coded in the coupled model. For wave refraction in the ice zone, a canonical study was conducted by Wadhams [2], who used offline calculations to estimate the refracted wavenumber. Since Dai [3] developed the coupled ocean-ice-wave system (online) based on the primitive equations, appropriate coding of wavenumber evolution could be demonstrated by the consistency between online and offline calculations. The second question is whether the primitive equation well reveals the real physics of wavenumber evolution during wave refraction, which can be verified with the consistency between the in situ observations and the online/offline calculation. To address these two questions, this paper is arranged as follows. In Section II, we introduce the in situ observations and numerical sensitivity experiments. In Section III, we analyze the theoretical estimate and the in situ observations. In Section IV, we provide a summary and identify future research topics.

II. INTRODUCTION TO OBSERVATIONAL DATA AND NUMERICAL EXPERIMENTS

A. INTRODUCTION TO THE IN SITU OBSERVATIONAL DATA

The in situ data used in this study were recorded by wave buoys from 30 September to 4 November 2015 in the Chukchi-Beaufort Seas and the western Arctic Ocean aboard the R/V Sikuliaq (SKQ) [17], [18]. The observations are supported by the project ''Sea State and Boundary Layer Physics of the Emerging Arctic Ocean'' and employ several advanced instruments, such as wave buoys and moorings. Three types of wave buoys (SWIFT [19], WB [20] and NIWA buoys) were used in these observations, which included 7 wave experiments (WE1, WE2, WE3, WE4, WE5, WE6, and WE7). Based on their descriptions [17], the NIWA data were abandoned because they do not include wavenumber information and the WB data were abandoned because they are interpolated onto the frequency domain of the SWIFT data, which may influence the accuracy of the wavenumber. As a result, the SWIFT data, which are provided in 30-minute segments, were selected for the present study. Among the 7 wave experiments, the number of SWIFT buoy pairs is much larger in the WE3 experiment than in other wave experiments. WE3 is the wave experiment carried out between October 12th, 2015, 22:19 UTC and October 13th, 2015, 22:12 UTC. After selection by Cheng [17], there are 131 buoy pairs in the WE3 experiment. The wavenumber (captured by SWIFT buoy) is determined by shipboard X-band Marine Radar, which samples the surface wave in space and time, therefore allowing a direct measurement of wavenumber evolution. Two buoys, which cover the frequencies greater than 0.0566 Hz and less than 0.4902 Hz with an increment of 0.0117 Hz, are included in each buoy pair, and they change locations every 30 minutes, with a maximum (minimum) distance of 85 (18) km between the two buoys (more information about their location is provided in the supplementary material). In most cases, one buoy is located in the open ocean, and the other buoy is located in the ice zone. Otherwise, the buoy pair was abandoned in our following analysis. Each buoy pair provides only 1 refracted wavenumber at a time, given a fixed frequency. The date, time, and location information of the buoy is shown in Table S1 of the supplementary material. To decrease the influence of observational error, we neglect observations in which the wavenumber increment is less than 0.3 percent of the incident wavenumber. After selection, the number of buoy pairs remains is 114. Advanced Microwave Scanning Radiometer 2 (AMSR2) and Soil Moisture and Ocean Salinity (SMOS) satellites, which are used in Cheng's work [17], are too coarse for our analysis. Instead, we estimate and verify the transient ice mass distribution based on offline calculations [2] in this study.

B. INTRODUCTION TO THE EXPERIMENTAL SETTINGS

The coupled ocean-ice-wave system, which includes a current model (the Regional Oceanic Modeling System (ROMS) [21]), a Wentzel-Kramers-Brillouin wave model [22] and a single-layer sea ice model [3], is employed in this study. The theoretical framework of the coupled ocean-ice-wave system is shown in Appendix A.

The coupled ocean-ice-wave system is configured for a 40 km $\times$ 20 km domain with a horizontal resolution of 1 km $\times$ 1 km. Our reason for this domain setting is as

follows. The distance between the buoy pair is from 18 km to 85 km. When buoys are closest to each other (18 km), both of the buoys are in the ice zone. Thus, the minimum ice zone should be set as 20 $km \times 20$ km. Assume open ocean covers the other half of this domain, the domain should be set as 40 $km \times 20$ km. There are 40 vertical grid levels spanning a total depth of 400 m (the grid level is larger in the lower layers and vice versa) in the ocean model following the work of Dai [3] because the experiment result is not sensitive to the variation in water depth in deep water [13]. Periodic boundaries are employed at the northern and southern boundaries in this study; however, there are open boundary conditions at the eastern and western boundaries. Follow Zhang [14], the reference water density is 1027.5 $kg \cdot m^{-3}$ based on observations in the Chukchi Sea and Beaufort Sea. The initial density, temperature and salinity are laterally uniform and vertically stratified with a buoyancy frequency of $N = 0.006\ s^{-1}$ in the mixed layer. In addition, the initial velocity is set to zero both for the ice and current. To better reveal the wavenumber evolution during wave refraction in the ice zone, the distribution of the ice field is supposed to remain constant, no wind stress is applied in this domain. At the ice boundary, the ice distribution (A_i) follows a hyperbolic function as in [3]:

$$A_i(x) = 0.4 + 0.4\frac{exp(x-5) - exp(5-x)}{exp(x-5) + exp(5-x)} \tag{1}$$

with a range of [0, 0.8] and is uniform along the edge. x is the distance to the ice edge, unit: km.

In the control experiment (denoted by Ctrl), the incident wave has an amplitude of 2 m, and the incident wavenumber is 0.45 m^{-1} (the incident wavelength is 14 m). In the propagation direction, the angle of incidence is set to 18.5° (which is nearly the smallest angle of incidence in the observation and produces a perfect consistency between online calculation and offline calculation; additional analysis is given in Sec III B). The ice thickness (h_i) is 0.04 m (maximum ice mass (m_i, $m_i = A_i \cdot h_i$) is 0.032 m, which is the greatest ice thickness in the observation). In the sensitivity experiments, most settings remain the same as those in the control experiment; however, we changed the variable under discussion. To determine the sensitivity to the angle of incidence, we set this angle to 45° (denoted by 1Tan), which is an angle of incidence found in the observation. For determining the ice thickness sensitivity, we set the ice thickness to 0.02 m (maximum ice mass is 0.016 m, which is the medium number in the observation; denoted by 16Mm). Additionally, for the mass loading model, the ice mass instead of ice thickness determines the wave refraction). For wavenumber amplitude sensitivity, we set the incident wavenumber to 0.9 m^{-1} (the incident wavelength is 7 m, denoted by Hfrq). For convenience, we define the notation for the sensitivity experiments in Table 1. All cases are integrated over 1 day, which is nearly the period that WE3 experiment was carried out. All the wave and ice parameters are based on the observations.

TABLE 1. Parameters used for the sensitivity experiments. In the control experiment, the total water depth of the ocean (denoted by H) was 400 *m*; the maximum ice mass (denoted by m_i) was 0.032 *m*; for the incident wave in the open ocean, the wave length (denoted by λ), wave amplitude (denoted by A) and the angle against the ice edge (incident angle, denoted by θ_i) were 14 *m*, 2 *m*, and 18.5°, respectively. For the sensitivity experiments, some parameters were changed. For example, the incidence angle is 45.0° in the 1Tan experiment, the wave length is only 7 *m* in the Hfrq experiment, and the maximum ice mass is only 0.016 *m* in the 16Mm experiment. However, the other parameters remained the same as those in the control experiment.

Name	H (m)	$\lambda(m)$	A (m)	$\theta_i(^\circ)$	$m_i(m)$
Ctrl	400	14	2	18.5	0.032
1Tan	400	14	2	45.	0.032
Hfrq	400	7	2	18.5	0.032
16Mm	400	14	2	18.5	0.016

III. RESULTS AND ANALYSIS

A. VARIATION OF WAVENUMBER IN MAGNITUDE DUE TO WAVE REFRACTION

The variation of wavenumber in magnitude (dk^2) during wave refraction is defined as $dk^2 = k_r^2 - k_i^2$, where k_r and k_i are the refracted wavenumber and incident wavenumber, respectively. With in situ observations, the incident wavenumber (in the open ocean) is estimated using the deep-water wave-dispersion relation and selected frequency [17] ($k_i = \omega^2/g$, where ω is the selected wave frequency, g is the gravitational acceleration, and k_i is the estimated incident wavenumber), while each buoy pair from the WE3 experiment provides 1 refracted wavenumber for a fixed frequency. Thus, we obtain an in situ dk^2 for a fixed frequency in each buoy pair.

On the other hand, refracted wavenumber could also be estimated with the offline calculation described by Wadhams [2]

$$k_r = \frac{k_i}{1 - m_i k_i \rho_i / \rho_w} \tag{2}$$

where ρ_i is the density of the ice, and ρ_w is the density of the water. This offline calculation is derived for the frazil-pancake ice zone, and was the same as the observation that was used [2]. According to the in situ data description, the transient ice mass is not captured by the buoy pairs, we suggest to estimate the ice mass with equation $m_i = \frac{\rho_w}{\rho_i}(\frac{1}{k_i} - \frac{1}{k_r})$, which is derived from Equation (2). Since waves in all frequencies undergo the same ice mass in a buoy pair, the ice mass estimated with wavenumbers at different frequencies should be consistent if the offline calculation is valid.

The results show that the estimated masses are quite consistent in each buoy pair (Fig. 1a) and strongly support our assumption. A further analysis is shown with the standard deviation of the estimated ice mass for each buoy pair in all 114 buoy pairs (Fig. 1b, red stars). The results suggested that most of standard deviations are smaller than 10 percent of the mean estimated ice mass. Furthermore, if we neglect the ice mass estimated with a small wavenumber (which is more easily to be influenced by the same observational error), the new

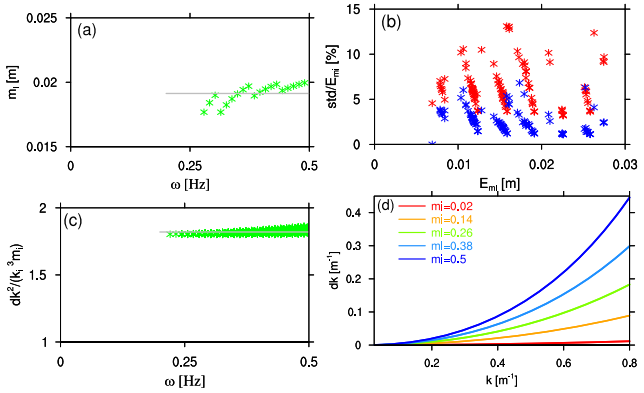

FIGURE 1. **(a) The ice mass (green stars, unit: *m*) is estimated for each incident frequency based on the observation from the buoy pair at 6:15 am October 12th, 2015 (more details can be found in Table. S1 of the supplemental material). The mean of the estimated mass is also presented (gray line). (b) The standard deviations (std) and mean of the estimated mass (Emi) at all 130 buoy pairs are presented (red stars). The standard deviations are also calculated (blue star) based on the estimated ice mass, which are greater than the mean of all the estimated masses. (c) The square of the wavenumber variation divided by the cube of the incident wavenumber times the ice mass (green stars) is calculated for each incident frequency at all 130 buoy pairs. The reference line (*y*=1.82) is also presented (gray line). (d) Given a constant ice mass of 0.02 *m* (red), 0.14 *m* (orange), 0.26 *m* (green), 0.38 *m* (blue) or 0.5 *m* (blue), the wavenumber increment is estimated for each incident wavenumber. Unit: m^{-1}.**

standard deviations are substantially smaller (Fig. 1b, blue stars), and most are nearly zero. Thus, we finally confirmed the validity of the offline calculation.

Substituting Equation (2) into the definition of variation of wavenumber in magnitude ($dk^2 = k_r^2 - k_i^2$), we have

$$\begin{aligned} dk^2 &= \left(\frac{1}{(1 - m_i k_i \rho_i/\rho_w)^2} - 1\right) k_i^2 \\ &= \frac{2 m_i k_i \rho_i/\rho_w - (m_i k_i \rho_i/\rho_w)^2}{(1 - m_i k_i \rho_i/\rho_w)^2} k_i^2 \\ &= \frac{2 m_i k_i^3 \rho_i/\rho_w}{1 - m_i k_i \rho_i/\rho_w} + \frac{(m_i \rho_i/\rho_w)^2 k_i^4}{(1 - m_i k_i \rho_i/\rho_w)^2} \end{aligned} \tag{3}$$

Because the ice mass is rather small in this study, $m_i k_i \rho_i/\rho_w \ll 1$ and $m_i k_i^3 \ll m_i^2 k_i^4$. Set $\rho_i = 910 kg/m^3$ and $\rho_w = 1027 kg/m^3$, $dk^2 \approx 1.82 m_i k_i^3$. Since the refracted wavenumber is provided in the observations, the incident wavenumber is estimated with the deep-water wave-dispersion relation ($k_i = \omega^2/g$), and we can estimate the ice mass ($m_i = \frac{\rho_w}{\rho_i}(\frac{1}{k_i} - \frac{1}{k_r})$) and the variation of wavenumber in magnitude ($dk^2 = k_r^2 - k_i^2$). The observations from the buoy pair suggest that $dk^2/m_i k_i^3$ is very close to 1.82 (Fig. 1c, green stars). As long as either the ice mass or the wavenumber remains small, this wave refraction relation is robust. However, if both the ice mass and wavenumber are large, wave reflection becomes nontrivial and cannot be ignored; wave reflection may even dominate in the wave-ice interactions.

Since the variation of wavenumber in magnitude is determined by the cube of the incident wavenumber and the variation in the ice mass, a larger incident wavenumber or ice mass variation leads to larger wavenumber variations. Offline calculation is employed to reveal the sensitivity of the wavenumber increment (defined as $dk = k_r - k_i$). Small ice mass variations cause no changes in the wavenumber increment (Fig. 1d red line), while the wavenumber increment can be more than half of the incident wavenumber with a larger ice mass variation (Fig. 1d blue line). First, we consider a constant wavenumber. If we nearly double the value of the ice mass from 0.14 *m* (Fig. 1d orange line) to 0.26 *m* (Fig. 1d green line), the wavenumber increment approximately increases from 0.1 m^{-1} to 0.2 m^{-1} with an incident wavenumber of 0.8 m^{-1} (the wavelength is 7.9 *m*), nearly doubling the wavenumber increment. Second, we consider a constant ice mass (e.g., $m_i = 0.38$ *m*, Fig. 1d dodger blue line). If we double the incident wavenumber from 0.4 m^{-1} (the wavelength is 15.8 *m*) to 0.8 m^{-1}, the wavenumber increment increases from 0.063 m^{-1} to 0.3 m^{-1}, which means that the wavenumber increment undergoes a nearly 4-fold increase (instead of doubling). In conclusion, the refracted wavenumber is quite sensitive to variations in the incident wavenumber.

After confirming the physical validity of the offline calculation, we also try to evaluate our coding of wavenumber evolution in the coupled ocean-ice-wave system (online model). The primitive equation for wavenumber evolution in the ice zone is written as

$$\frac{\partial \vec{k}}{\partial t} + \vec{c_g} \cdot \nabla_\perp \vec{k} = -\vec{k} \nabla_\perp \vec{V} + \frac{k \rho_i}{2 \rho_w} \frac{\sqrt{gk}}{(1 + B_0 k)^{3/2}} \cdot \nabla_\perp m_i \tag{4}$$

where $\vec{k}$ and k are the wavenumber vector and the magnitude, respectively, and $\vec{c_g}$ is the group velocity vector, $\vec{V}$ is the background flow vector, and $B_0 = (\rho_i/\rho_w) m_i$. Assuming that the y direction is perpendicular to the ice mass gradient ($\frac{\partial m_i}{\partial y} = 0$), the wave field reaches equilibrium in a very short period ($\frac{\partial}{\partial t} = 0$), and the background flow is rather small compared with the group velocity

$$c_{gx} \frac{\partial k_x}{\partial x} = \frac{k \rho_i}{2 \rho_w} \frac{\sqrt{gk}}{(1 + m_i k \rho_i/\rho_w)^{3/2}} \frac{\partial m_i}{\partial x} \tag{5}$$

The group velocity in the x direction is written as

$$c_{gx} = \frac{g k_x}{2k(1 + m_i k \rho_i/\rho_w)^{3/2} \sqrt{gk}} \tag{6}$$

Thus,

$$\frac{\partial k_x^2}{\partial x} = \frac{2 \rho_i}{\rho_w} k^3 \frac{\partial m_i}{\partial x} \tag{7}$$

Since there is no wavenumber variation in the y direction, over an infinitesimal distance,

$$\delta k^2 = \delta k_x^2 = \frac{2 \rho_i}{\rho_w} k^3 dm_i \tag{8}$$

where δk^2 (δk_x^2) is the wavenumber (in the x-direction) evolution over a given distance in the ice zone, with an ice mass variation of dm_i. If this distance is considered from the ice

edge to the current location inside the ice zone, Equation (8) should be equal to $dk^2 = \frac{2\rho_i}{\rho_w} k_i^3 m_i$. The wavenumber in the open ocean/ice zone, which is integrated in the sensitivity experiments with the online model, (Fig. 2, red lines) is very consistent with the refracted wavenumbers estimated with the offline calculations (Fig. 2, blue lines), both of which used the same ice mass distribution and incident wavenumber (in the open ocean). Decrease the partition of k_x by decreasing the angle of incidence from 18.5° (Fig. 2a) to 45° (Fig. 2b), the wavenumber increment remains nearly the same. However, if the incident wavenumber doubles (Fig. 2c), the wavenumber increment increases significantly. The wavenumber increment also increases due to doubling the ice mass from Fig. 2d to Fig. 2a, though the wave increment increases more by doubling the incident wavenumber. The consistency between the offline calculation and the online model confirms that our coding of wavenumber evolution in magnitude is appropriate in the coupled ocean-ice-wave system.

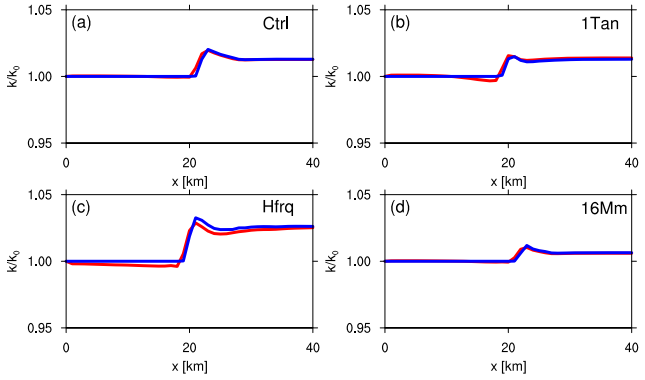

FIGURE 2. The distribution of the wavenumber in the (a) Ctrl experiment, (b) 1Tan experiment, (c) Hfrq experiment, and (d) 16Mm experiment. The wavenumber is divided by the incident wavenumber. Red lines show the results from the online model, and blue lines are the estimates from the offline calculations.

B. VARIATION IN WAVE PROPAGATING DIRECTION DUE TO REFRACTION

As the waves penetrate into the ice zone, the wave changes both in magnitude of wavenumber and in propagating direction due to refraction. The variation in the wave propagating direction ($\delta\theta$) is defined as the difference between angle of incidence (θ_i) and angle of refraction (θ_r). Thus, we have $\delta\theta = |\theta_r - \theta_i| = \theta_i - \theta_r$, since if the wave propagates from the open ocean to the ice zone, $\theta_i > \theta_r$.

According to Snell's law,

$$sin\theta_r = \frac{k_i sin\theta_i}{k_r} = (1 - m_i k_i \frac{\rho_i}{\rho_w}) sin\theta_i \tag{9}$$

The angle of refraction (θ_r) is determined by the incident wavenumber, refracted wavenumber and angle of incidence (θ_i) [2]. Since the refracted wavenumber is determined by the variations in the ice mass and the incident wavenumber, the angle of refraction is determined by the incident wavenumber, the variation in the ice mass and the angle of incidence. The larger the angle of incidence is, the larger the angle of refraction is. Therefore are the incident wavenumber and the ice mass.

Is this conclusion also suitable for the deflection? Substituting the definition of deflection into Equation (9), the deflection ($\delta\theta = \theta_i - \theta_r$) is written as

$$sin\delta\theta = \frac{2sin\theta_i}{\sqrt{\frac{1}{k_i m_i} + 2}(\sqrt{\frac{cos^2\theta_i}{k_i m_i} + 2} + \frac{cos\theta_i}{\sqrt{k_i m_i}})} \tag{10}$$

A larger angle of incidence leads to a larger value of $sin\theta_i$ and a smaller value of $cos\theta_i$, resulting in a larger deflection. On the other hand, a larger incident wavenumber or ice mass variation also increases $sin\delta\theta$, which in turn leads to a larger deflection.

To verify the conclusion drawn above, observational data from the WE3 experiment is employed here, since one of the buoys is in the open ocean, while the other is in the ice zone. However, the in situ observational data only provide the direction of wave propagation, without any information about the tangent direction of the interface. We suggest a method to estimate the real angle of incidence and angle of refraction. Define the angle between the eastward direction (Fig. 3, black vector) and propagating direction of the incident wave (Fig. 3, red vector) as $\theta_{i(abs)}$, define the angle between the eastward direction and the propagating direction of refracted wave (Fig. 3, green vector) as $\theta_{r(abs)}$, and define the angle between the tangent of the ice edge (Fig. 3, purple vector) and the eastward direction as θ_m. Four basic scenarios are considered as follows (Fig. 3).

(1) $0 \le \theta_{r(abs)} \le \theta_{i(abs)} \le 90°$

Based on the angles defined in Fig. 3a,

$$\theta_r - \theta_{r(abs)} + \theta_m = 90° \tag{11}$$

$$\theta_i - \theta_{i(abs)} + \theta_m = 90° \tag{12}$$

According to Snell's law

$$\frac{sin\theta_i}{sin\theta_r} = \frac{k_r}{k_i} \tag{13}$$

Substituting Equations (11) and (12) for Equation (13), we have

$$\theta_m = acrtan(\frac{cos\theta_{i(abs)} - \frac{k_r}{k_i} cos\theta_{r(abs)}}{\frac{k_r}{k_i} sin\theta_{r(abs)} - sin\theta_{i(abs)}}) \tag{14}$$

Then, the angle of incidence (θ_i) and angle of refraction (θ_r) can be calculated by including θ_m in Equations (11) and (12).

(2) $0 \le \theta_{i(abs)} \le \theta_{r(abs)} \le 90°$

Based on the angles defined in Fig. 3b,

$$\theta_r + \theta_{r(abs)} + \theta_m = 90° \tag{15}$$

$$\theta_i + \theta_{i(abs)} + \theta_m = 90° \tag{16}$$

Substituting Equations (15) and (16) for Equation (13), we have

$$\theta_m = acrtan(\frac{cos\theta_{i(abs)} - \frac{k_r}{k_i} cos\theta_{r(abs)}}{sin\theta_{i(abs)} - \frac{k_r}{k_i} sin\theta_{r(abs)}}) \tag{17}$$

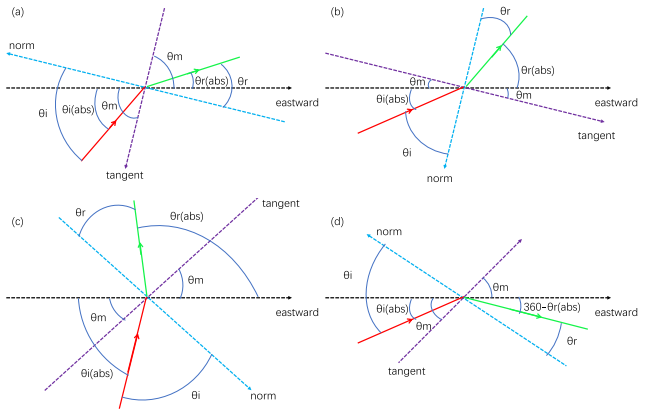

FIGURE 3. Four possible scenarios of wave refraction during observation are presented. The black vector presents the eastward direction, which is defined as the reference direction. The purple vector presents the tangent direction of the ice edge. The blue vector presents the direction of norm at the interface. The red vector presents the propagating direction of incident wave. The green vector presents the propagation direction of the refracted wave. Thus, the angle between tangent direction and the reference direction is called the rotation of tangent direction and is denoted as θ_m. The angle between the direction of incident wave propagation and the direction of norm at the interface is the angle of incidence and is denoted as θ_i, while the angle between the direction of refracted wave propagation and the direction of norm at the interface is the angle of refraction and is denoted as θ_r. The angle between the reference direction and the direction of incident wave propagation is called absolute direction of the incident wave propagation and is denoted as $\theta_{i(abs)}$, while the angle between the reference direction and the direction of refracted wave propagation is called absolute direction of refracted wave propagation and is denoted as $\theta_{r(abs)}$. The scenario in which $0 \le \theta_{r(abs)} \le \theta_{i(abs)} \le 90°$ is shown in (a), the scenario in which $0 \le \theta_{i(abs)} \le \theta_{r(abs)} \le 90°$ is shown in (b), the scenario in which $0 \le \theta_{i(abs)} \le 90° \le \theta_{r(abs)} \le 180°$ is shown in (c), and the scenario in which $0 \le \theta_{i(abs)} \le 90°\&270° \le \theta_{r(abs)} \le 360°$ is shown in (d).

Then, the angle of incidence (θ_i) and angle of refraction (θ_r) can be calculated by including θ_m in Equations (15) and (16).

(3) $0 \le \theta_{i(abs)} \le 90° \le \theta_{r(abs)} \le 180°$

Based on the angles defined in Fig. 3c,

$$\theta_{r(abs)} + \theta_r - \theta_m = 90° \tag{18}$$

$$\theta_{i(abs)} + \theta_i - \theta_m = 90° \tag{19}$$

Substituting Equations (18) and (19) for Equation (13), we have

$$\theta_m = acrtan(\frac{cos\theta_{i(abs)} - \frac{k_r}{k_i} cos\theta_{r(abs)}}{\frac{k_r}{k_i} sin\theta_{r(abs)} - sin\theta_{i(abs)}}) \tag{20}$$

Then, the angle of incidence (θ_i) and angle of refraction (θ_r) can be calculated by including θ_m in Equations (18) and (19).

(4) $0 \le \theta_{i(abs)} \le 90°\&270° \le \theta_{r(abs)} \le 360°$

Based on the angles defined in Fig. 3d,

$$360° - \theta_{r(abs)} + \theta_r + \theta_m = 90° \tag{21}$$

$$\theta_i - \theta_{i(abs)} + \theta_m = 90° \tag{22}$$

Substituting Equations (21) and (22) for Equation (13), we have

$$\theta_m = acrtan(\frac{cos\theta_{i(abs)} - \frac{k_r}{k_i} cos\theta_{r(abs)}}{\frac{k_r}{k_i} sin\theta_{r(abs)} - sin\theta_{i(abs)}}) \tag{23}$$

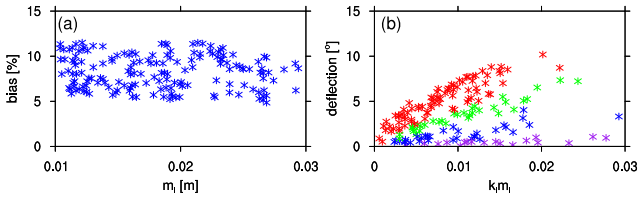

FIGURE 4. Deflection bias, which is defined as the differences in deflection between in situ observation and offline calculation divided by the deflection, are shown as blue stars in (a). Unit: %. Deflections with angles of incidence [85°, 90°), [80°, 85°), [50°, 80°), and [18°, 50°) are shown as red stars, green stars, blue stars and purple stars in (b), respectively. Unit:°.

Then, the angle of incidence (θ_i) and angle of refraction (θ_r) can be calculated by including θ_m in Equations (21) and (22).

With Snell's law, the deflection should be smaller than 90°, since both k_r and k_i are positive. On the other hand, if there are other scenarios, we can also make it one of the four scenarios above by rotating the vectors in an angle of $n \times 90°$, where n is integer.

Substituting $dk^2 = 1.82 m_i k_i^3$ into Equation (10), the deflection estimated with the incident wavenumber, refracted wavenumber, and angle of incidence is called the offline calculation, while the deflection calculated with the four scenarios above is called in the situ observation. For the in situ observations, we assume buoy 1 is in the open ocean while buoy 2 is in the ice zone. When we encounter the opposite situation, buoy 1 is in the ice zone, buoy 2 is in the open ocean, and the estimated θ_i would be smaller than θ_r and is abandoned. We also neglect the observations when m_i is smaller than 0.01 m. Still, both θ_i and θ_r should be smaller than 90°. After our selection, there are only 165 in situ observation selected from 131 buoy pairs, with 37 types of frequency in each buoy pair, which means 96.6 percents of the observations are abandoned. Deflection bias (Fig. 4a, blue stars), which is defined as differences of deflection between in situ observation and offline calculation divide by the deflection, are smaller than 10% in the observations. The consistence between the in situ observation and offline calculation confirms the physical validity of the offline calculation. For the deflection features, we found that the deflections, whose angles of incidence are between 85° and 90° (red stars) are larger than those whose angles of incidence are between 80° and 85° (green stars). The deflections, whose angles of incidence are between 50° and 80° (blue stars) are larger than those whose angles of incidence are between 18° and 50° (purple stars). With a similar angle of incidence (stars with the same color), a larger wavenumber and ice mass ($k_i m_i$) will induce a larger deflection.

After confirming the physical validity of the offline calculation, we also try to evaluate our coding of wave propagating direction in the coupled ocean-ice-wave system (online model). To reproduce these conclusions drawn by offline calculation with the online model, we use wavenumber evolution equation (Equation (4)). As in the above discussion, the x (y) direction is defined as along (against) the ice mass gradient.

Additionally, $sin\theta_i = k_y/k_i$ ($k_i = k$ in the open ocean) and $sin\theta_r = k_y/k_r$ ($k_r = k$ in the ice zone).

Thus, the deflection ($\delta\theta$) is rewritten as

$$\begin{aligned} sin\delta\theta &= sin(\theta_i - \theta_r) \\ &= sin\theta_i\sqrt{1 - sin^2\theta_r} - sin\theta_r\sqrt{1 - sin^2\theta_i} \\ &= k_y/k_i\sqrt{1 - k_y^2/k_r^2} - k_y/k_r\sqrt{1 - k_y^2/k_i^2} \\ &= \frac{1}{k_r k_i}\frac{k_y(k_r^2 - k_i^2)}{\sqrt{k_r^2 - k_y^2} + \sqrt{(k_i^2 - k_y^2)}} \end{aligned} \tag{24}$$

Because $k_r^2 - k_i^2 \approx 2m_i k^3$, $k_r k_i = k_i^2\sqrt{1 + 2m_i k_i}$, and

$$sin\delta\theta \approx \frac{2m_i k_i k_y}{\sqrt{1 + 2k_i m_i}\sqrt{k_i^2 + 2k_i^3 m_i - k_y^2}} \tag{25}$$

Then, dividing both the numerator and denominator by $m_i k^2$, we obtain

$$sin\delta\theta \approx \frac{2sin\theta_i}{\sqrt{\frac{1}{k_i m_i} + 2}\sqrt{\frac{cos^2\theta_i}{k_i m_i} + 2}} \tag{26}$$

Equations (10) and (26) do not seem to be consistent, since we made an approximation by assuming $\delta k_i^2 = 2m_i k_i^3$, whose complete equation is represented by Equation (3). However, when we check the results of online (Fig. 5, red line) and offline calculations (Fig. 5, blue line), the deflections are nearly the same. When the angle of incidence increases, the deflection increases (Fig. 5a, b). When the incident wavelength becomes shorter (Fig. 5c), which means that the wavenumber increases, the deflection increases. When the ice mass decreases (Fig. 5d), the deflection increases as well.

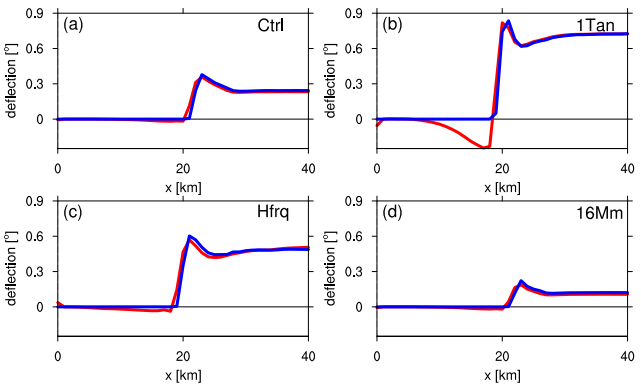

FIGURE 5. The distribution of the deflection in the (a) Ctrl experiment, (b) 1Tan experiment, (c) Hfrq experiment, and (d) 16Mm experiment. Red lines show the results from the online model, and blue lines are the estimates from the offline calculations. Unit:°.

However, we do find a significant deflection bias immediately before the wave propagates into ice zone (Fig. 5b, red line) in the online calculation. This is not an incorrect estimate, and the bias is induced due to the influence of advection term in wavenumber evolution equation (Equation (3)), which is also discussed in [3]. Due to the positive gradient of wavenumber on the right side of the ice edge, the wavenumber on the left side of the ice edge decreases due to the negative influence from advection term, and lead to a larger angle $arcsin(k_y/k)$. Since the wavenumber is induced by the advection term, it cannot be estimated by the offline calculation. However, deflection bias only occurs on the left side of the ice edge; thus, all the wavenumbers and deflection in the ice zone are consistent between the online calculation and offline calculation. Another issue should be kept in mind, in which the deflection bias extends a distance of nearly 12 *km*, which will not include longer distance given a larger deflection [3]. As a result, the buoy in the open ocean should be kept farther than 15 *km* from the ice edge. Fortunately, buoys in the open ocean from all the 165 observations we selected are farther than 15 *km* from the ice edge.

IV. SUMMARY AND DISCUSSION

In this study, wave-ice interactions in an MIZ are investigated using in situ observations, offline calculations and a numerical model. When surface gravity waves propagate into the ice zone, they reflect and refract at the ice boundary. However, based on the assumption that the ice is thin, reflection is neglected. As the waves penetrate the ice zone, the wavenumber becomes larger, while the angle of refraction decreases. In this study, we discussed several aspects of the refraction process in more detail than was discussed in previous studies.

First, we focus on the wavenumber evolution (both magnitude and propagating direction) in this study instead of wave energy evolution as in previous studies. We verify the physical validity of the offline calculation for wave refraction in the ice zone by consistency between the in situ observations and estimates from offline calculation. We also test the reliability of coding in our online calculation by consistence between offline calculation and online simulation. In conclusion, our coupled ocean-ice-wave model can well describe the wave evolution in the ice zone.

Second, the variation of wavenumber in magnitude (dk^2) during refraction is proportional to the cube of the incident wavenumber (k_i^3) and linearly proportional to the ice mass variation (m_i). As a result, the variation in magnitude of wavenumber is more sensitive to the incident wavenumber than to the ice mass. On the other hand, shorter waves, thicker ice floes and larger angles of incidence lead to larger angles of refraction and larger deflection.

Third, the online model indicates that we need to be careful, when placing the instrument in the open ocean. There is deflection bias immediately before the wave propagates into the ice zone due to the advection term of the wavenumber evolution equation. We need to keep the instrument 15 *km* or farther from the ice edge to obtain a more general state of the open ocean.

The purpose of this paper was to verify the physical validity and coding reliability of our online model. To achieve this goal, we propose a method to find the real angle of incidence and angle of refraction from the observational data. We also propose and verify serval methods for variable estimation, which allow us to obtain accurate information more easily.

APPENDIX A
DEFINITIONS OF SYMBOLS

Symbol	Name	Defined in Section
A_i	ice concentration	II.B
B_0	defined constant	III.A
$\vec{c_g}$	group velocity vector	III.A
c_{gx}	group velocity in the x direction	III.A
dk	wavenumber increment	III.A
dk^2	variation of wavenumber in magnitude	III.A
dm_i	variation of ice mass	III.A
δk^2	variation of wavenumber in the online model	III.A
δk_x^2	variation of wavenumber in the online model	III.A
$\delta\theta$	deflection	III.B
g	gravitational acceleration	III.A
h_i	ice thickness	II.B
$\vec{k}$	wavenumber vector	III.A
k	wavenumber magnitude	III.A
k_i	incident wavenumber	III.A
k_r	refracted wavenumber	III.A
k_x	wavenumber in the cross-ice-edge direction	III.A
m_i	ice mass	II.B
N	buoyancy frequency	II.B
ω	wave frequency	III.A
ρ_i	ice density	III.A
ρ_w	water density	III.A
θ_i	angle of incidence	III.B
$\theta_{i(abs)}$	propagating direction of incident wave	III.B
θ_m	angle between the tangent of the ice edge and the eastward direction	III.B
θ_r	angle of refraction	III.B
$\theta_{r(abs)}$	propagating direction of refracted wave	III.B
θ_r	angle of refraction	III.B
$\vec{\overline{V}}$	background flow vector	III.A
x	distance in the cross-ice edge direction	II.B
y	distance in the along-ice edge direction	III.A

Finally, we find that care must be taken when placing the instrument in the open ocean, in order to obtain a more general information about the open ocean. With wavenumber evolution (this study), wave energy evolution [3], [13], submesoscale ocean dynamics [14] and ice dynamics [12] being verified, our coupled ocean-ice-wave model appear to be a reliable model for polar ocean simulation, after the thermodynamics of the sea ice are verified in our future work.

APPENDIX B
THEORETICAL FRAMEWORK OF THE COUPLED OCEAN-ICE-WAVE SYSTEM

Based on the discussion in [3], the theoretical framework of the coupled ocean-ice-wave system is as follows. Ocean model

$$\frac{\partial\vec{v}}{\partial t}+(\vec{v}\cdot\nabla_\perp)\vec{v}=-\nabla_\perp\Phi-f\vec{z}\times\vec{v}+(1-A_i)\vec{\tau}_{aw}-A_i\vec{\tau}_{wi}+\vec{F}^w+\vec{J}-\nabla_\perp\Gamma \tag{27}$$

$$\frac{\partial\Phi}{\partial z}+\frac{g\rho_w}{\rho_0}=-\frac{\partial\Gamma}{\partial z}+K \tag{28}$$

$$\nabla\cdot\vec{v}=0 \tag{29}$$

$$\frac{\partial c}{\partial t}+(\vec{v}\cdot\nabla)c=c^w+D^c+Q^c \tag{30}$$

Sea ice model

$$\rho_i m_i\left(\frac{\partial\vec{v}_i}{\partial t}+(\vec{v}_i\cdot\nabla)\vec{v}_i\right)=-\rho_i m_i f\vec{z}\times\vec{v}_i+A_i(\vec{\tau}_{ai}+\vec{\tau}_{wi})+\vec{F}_i+\vec{F}_r \tag{31}$$

$$\frac{\partial A_i}{\partial t}+\nabla\cdot(\vec{v}_i A_i)=0(0\le A_i\le 1) \tag{32}$$

$$\frac{\partial m_i}{\partial t}+\nabla\cdot(\vec{v}_i m_i)=0 \tag{33}$$

Wave model

$$\frac{\partial\vec{k}}{\partial t}+(\vec{c_g}\cdot\nabla)\vec{k}=\frac{k\rho_i}{2\rho_w}\frac{\sqrt{gk}}{(1+B_0k)^{3/2}}\cdot\nabla_\perp M_i-\vec{k}\nabla_\perp\vec{\overline{V}} \tag{34}$$

$$\frac{\partial\Lambda}{\partial t}+\nabla\cdot(\vec{c_g}\Lambda)=-(1-A_i)\frac{\epsilon_b}{\omega_0}+A_i\alpha c_g\Lambda \tag{35}$$

$\vec{v}=(u,v,w)$ is the current velocity vector, and u, v and w are the current velocities in x, y and z directions, respectively. Φ is the sea surface potential function. f is the Coriolis parameter; here, we use $f=0.00014$. F^w is a wave-induced nonconservative force. J and K represent the horizontal and vertical components of the vortex force, respectively. Γ is the Bernoulli head. c is the tracer, c^w is the wave-induced effect on the tracer, and is the tracer diffusion. Q^c is the source of the tracer. $\vec{v}_i=(u_i,v_i)$ is the sea ice velocity vector, and u_i and v_i are the ice velocities in the x and y directions, respectively. F_i is the internal stress of the ice. F_r is the wave radiation stress exerted on the sea ice. τ_{ai} and τ_{aw} are the wind stresses exerted on the sea ice and the current, respectively. is the interfacial stress between the ocean and the ice. ρ_i, ρ_w and ρ_0 are the ice density, water density and reference density, respectively.

$\vec{k}$ and $\vec{c_g}$ are the wavenumber and group velocity vectors, respectively. $\vec{V}$ is the depth-averaged current velocity vector. $\Lambda = E_w/\omega_0$ is the wave action, E_w is the depth-integrated wave energy density, ω_0 is the intrinsic wave frequency, and ϵ_b is the dissipation rate due to the wave breaking in open water, and α is the wave energy decay rate as the wave propagates through the ice field.

ACKNOWLEDGMENT

The authors are grateful to Dr. Thomson and his collaborators for sharing the observational data.

REFERENCES

[1] M. H. Meylan, L. G. Bennetts, J. E. M. Mosig, W. E. Rogers, M. J. Doble, and M. A. Peter, "Dispersion relations, power laws, and energy loss for waves in the marginal ice zone," *J. Geophys. Res., Oceans*, vol. 123, no. 5, pp. 3322–3335, May 2018, doi: 10.1002/2018JC013776.

[2] P. Wadhams and B. Holt, "Waves in frazil and pancake ice and their detection in Seasat synthetic aperture radar imagery," *J. Geophys. Res.*, vol. 96, no. 5, pp. 8835–8852, May 1991, doi: 10.1029/91JC00457.

[3] H.-J. Dai, J. C. McWilliams, and J.-H. Liang, "Wave-driven mesoscale currents in a marginal ice zone," *Ocean Model.*, vol. 134, pp. 1–17, Feb. 2019, doi: 10.1016/j.ocemod.2018.11.006.

[4] Q. Liu, W. E. Rogers, A. Babanin, J. Li, and C. Guan, "Spectral modeling of ice-induced wave decay," *J. Phys. Oceanogr.*, vol. 50, no. 6, pp. 1583–1604, Jun. 2020, doi: 10.1175/JPO-D-19-0187.1.

[5] X. Zhao and H. H. Shen, "Ocean wave transmission and reflection by viscoelastic ice covers," *Ocean Model.*, vol. 92, pp. 1–10, Aug. 2015, doi: 10.1016/j.ocemod.2015.05.003.

[6] L. Wu, Ø. Breivik, and A. Rutgersson, "Ocean-wave-atmosphere interaction processes in a fully coupled modeling system," *J. Adv. Model. Earth Syst.*, vol. 11, no. 11, pp. 3852–3874, Nov. 2019, doi: 10.1029/2019MS001761.

[7] G. Boutin, F. Ardhuin, D. Dumont, C. Sévigny, F. G. Ardhuin, and M. Accensi, "Floe size effect on wave-ice interactions: Possible effects, implementation in wave model, and evaluation," *J. Geophys. Res., Oceans*, vol. 123, no. 7, pp. 4779–4805, Jul. 2018, doi: 10.1029/2017JC013622.

[8] F. Montiel, V. A. Squire, and L. G. Bennetts, "Attenuation and directional spreading of ocean wave spectra in the marginal ice zone," *J. Fluid Mech.*, vol. 790, pp. 492–522, Mar. 2016, doi: 10.1017/jfm.2016.21.

[9] P. K. Bhaskaran, "Challenges and future directions in ocean wave modeling a review," *J. Extre. Eve.*, vol. 6, no. 2, Nov. 2019, Art. no. 195004, doi: 10.1142/S2345737619500040.

[10] A. L. Kohout, M. J. M. Williams, S. M. Dean, and M. H. Meylan, "Storm-induced sea-ice breakup and the implications for ice extent," *Nature*, vol. 509, pp. 604–609, May 2014, doi: 10.1038/nature13262.

[11] A. K. Peterson, I. Fer, M. G. McPhee, and A. Randelhoff, "Turbulent heat and momentum fluxes in the upper ocean under arctic sea ice," *J. Geophys. Res., Oceans*, vol. 122, no. 2, pp. 1439–1456, Feb. 2017, doi: 10.1002/2016JC012283.

[12] H. Dai, J. Cui, and J. Yu, "Revisiting mesoscale eddy genesis mechanism of nonlinear advection in a marginal ice zone," *Acta Oceanologica Sinica*, vol. 36, no. 11, pp. 14–20, Nov. 2017, doi: 10.1007/s13131-017-1134-8.

[13] X. Zhang, H. Dai, J. Zhao, and H. Yin, "Sensitivity study of the wave-driven current in an arctic frazil-pancake ice zone," *Acta Oceanologica Sinica*, vol. 39, no. 3, pp. 123–129, Mar. 2020, doi: 10.1007/s13131-020-1560-x.

[14] X. Zhang, H. Dai, J. Zhao, and H. Yin, "Generation mechanism of an observed submesoscale eddy in the chukchi sea," *Deep Sea Res. I, Oceanographic Res. Papers*, vol. 148, pp. 80–87, Jun. 2019, doi: 10.1016/j.dsr.2019.04.015.

[15] J. Thomson, "Emerging trends in the sea state of the beaufort and chukchi seas," *Ocean Model.*, vol. 105, pp. 1–12, Sep. 2016, doi: 10.1016/j.ocemod.2016.02.009.

[16] Y. Wang, B. Holt, W. Erick Rogers, J. Thomson, and H. H. Shen, "Wind and wave influences on sea ice floe size and leads in the beaufort and chukchi seas during the summer-fall transition 2014," *J. Geophys. Res., Oceans*, vol. 121, no. 2, pp. 1502–1525, Feb. 2016, doi: 10.1002/2015JC011349.

[17] S. Cheng, W. E. Rogers, J. Thomson, M. Smith, M. J. Doble, P. Wadhams, A. L. Kohout, B. Lund, O. P. G. Persson, C. O. Collins, S. F. Ackley, F. Montiel, and H. H. Shen, "Calibrating a viscoelastic sea ice model for wave propagation in the arctic fall marginal ice zone," *J. Geophys. Res., Oceans*, vol. 122, no. 11, pp. 8770–8793, Nov. 2017, doi: 10.1002/2017JC013275.

[18] J. Thomson, J. Talbert, A. de Klerk, A. Brown, M. Schwendeman, J. Goldsmith, J. Thomas, C. Olfe, G. Cameron, and C. Meinig, "Biofouling effects on the response of a wave measurement buoy in deep water," *J. Atmos. Ocean. Technol.*, vol. 32, no. 6, pp. 1281–1286, Jun. 2015, doi: 10.1175/JTECH-D-15-0029.1.

[19] J. Thomson, "Wave breaking dissipation observed with SWIFT drifters," *J. Atmos. Ocean. Technol.*, vol. 29, no. 12, pp. 1866–1882, Dec. 2012, doi: 10.1175/JTECH-D-12-00018.1.

[20] M. J. Doble, G. De Carolis, M. H. Meylan, J. Bidlot, and P. Wadhams, "Relating wave attenuation to pancake ice thickness, using field measurements and model results," *Geophys. Res. Lett.*, vol. 42, no. 11, pp. 4473–4481, Jun. 2015, doi: 10.1002/2015GL063628.

[21] A. F. Shchepetkin and J. C. McWilliams, "The regional oceanic modeling system (ROMS): A split-explicit, free-surface, topography-following-coordinate oceanic model," *Ocean Model.*, vol. 9, no. 4, pp. 347–404, Jan. 2005, doi: 10.1016/j.ocemod.2004.08.002.

[22] Y. Uchiyama, J. C. McWilliams, and A. F. Shchepetkin, "Wave–current interaction in an oceanic circulation model with a vortex-force formalism: Application to the surf zone," *Ocean Model.*, vol. 34, nos. 1–2, pp. 16–35, Jan. 2010, doi: 10.1016/j.ocemod.2010.04.002.

HAIJIN DAI received the B.S. degree in meteorology from Nanjing University, Nanjing, China, in 2009, and the Ph.D. degree in meteorology from Peking University, Beijing, China, in 2015.

Since 2015, he has been an Assistant Researcher with the College of Meteorology and Oceanography, National University of Defense Technology. He has been a Postdoctoral Fellow with the College of Oceanic and Atmospheric Sciences, Ocean University of China, since 2019. He is the author of more than 14 articles that have been published in top journals, such as "*Climate Dynamics*," "*Ocean Modelling*," "*Deep-Sea Research Part I*," "*Remote Sensing*," "*Journal of Atmospheric and Oceanic Technology*," "*Acta Oceanologica Sinica*," "*Advances in Meteorology*," and "*Journal of Meteorological Research*." His research interests include ocean modeling, ice modeling, mesoscale eddies, ocean circulation, meridional heat transport, and climate change.

Dr. Dai was invited to give an oral presentation at the annual meeting of the American Geophysical Union, which is the summit meeting in the discipline of Earth Science around the world. He was also invited to give an oral presentation at the annual meeting of Ocean University of China in the same year. He gave an oral presentation (online) at the meeting of the Joint JpGU-AGU meeting, in June 2020.

JUN ZHAO received the B.S. degree in mathematics science and the M.S. and Ph.D. degrees in computer science from the National University of Defense Technology, Changsha, China, in 1994, 1997, and 2007, respectively.

Since 1997, he has been a Teacher with the National University of Defense Technology, where he is currently a Professor with the College of Meteorology and Oceanography. He is the author of more than 30 articles that have been published in top journals, such as "*Deep-Sea Research Part I*," "*Acta Oceanologica Sinica*," and "*Journal of Meteorological Research*." His research interests include numerical modeling and high performance computing.

Prof. Zhao was invited to give presentations at the meetings SC2009 (Germany), AGU 2017 (USA), and EGU2019 (Austria).

XUEYAN ZHANG received the B.S. degree in meteorology from the Ocean University of China, Qingdao, China, in 2017, and the M.S. degree in computer science from the National University of Defense Technology, Changsha, China, in 2020.

Since 2020, she has been a Teacher with the College of Meteorology and Oceanography, National University of Defense Technology. She is the author of more than three articles that have been published in top journals, such as "*Deep-Sea Research Part I*" and "*Acta Oceanologica Sinica*." Her research interests include mesoscale eddy genesis and wave-ice interaction.